Analysis of geometrical defects in overhang fabrications in electron beam melting based on thermomechanical simulations and experimental validations

Soukaina Ghaoui, Yann Ledoux, Frédéric Vignat, Matthieu Museau, Thanh Hoang Vo, François Villeneuve, Alex Ballu

Analysis of geometrical defects in overhang fabrications in Electron Beam Melting based on thermomechanical simulations and experimental validations

S. Ghaoui[1*], Y. Ledoux[1], F. Vignat[2], M. Museau[2], T.H. Vo[2], F. Villeneuve[2], A. Ballu[1]

[1] Univ. Bordeaux, I2M, UMR 5295, F-33400 Talence, France

[2] Univ. Grenoble Alpes, CNRS, Grenoble INP, G-SCOP, F-38000 Grenoble

*(Corresponding author: soukaina.ghaoui@u-bordeaux.fr)

Keywords

Abstract

Electron Beam Melting is an innovative process for the production of massive parts with minimum support structures and negligible residual stress. However, some geometries, such as overhang volumes, still pose a challenge to manufacture and can result in non-negligible geometrical defects such as "side loss". Based on thermomechanical simulations, the aim of this work is to understand the reasons for the appearance of this defect and its evolution throughout successive layer depositions. Simulation results indicate that side loss is due to the repetitive force applied by the new layers on the previous ones due to the fast shrinkage in the top of the part. In addition, both simulation and experimental analysis show an increase in the defect amplitude with increasing thickness of the overhang volume and its stabilization after the first millimeters of the overhang volume.

1. Introduction

Electron Beam Melting (EBM) is a recent powder bed fusion process, relevant for manufacturing complex geometries. These manufactured parts have good mechanical properties with a relatively accurate geometry. The principle of this process is based on successive additions of powder layers on a base plate, and their selective melting by an electron beam. The nature of the process requires conductive materials to produce the parts [1]; the standard materials recommended by the manufacturer ARCAM AB are Titanium alloys Ti6Al4V (also known as TA6V), Ti6Al4V ELI or Titanium Grade 2. Other alloys are also used, like Cobalt-Chrome ASTM F75 or Inconel 718 [2].

Whatever alloys are selected for production, the parts present different types of defects due to complex and coupled thermomechanical phenomena that occur during fabrication. For powder bed fusion processes, Malekipour and Elmounayri [3] have classified defects into four categories according to their observation scale: geometric and dimensional inaccuracies, defects related to surface quality, microstructure and mechanical properties. One of the main challenges to upscaling the EBM process from the laboratory to industrial applications requires predicting and improving the geometrical quality of the produced parts. This salient point corresponds to the main focus of the present paper.

Geometrical defects can be located on different zones of the parts and mainly result from thermal deformations of the geometry coupled with the successive depositions of material. There are

empirical rules to guide the manufacturer in identifying the most suitable process parameters; however, in some cases it is difficult to limit geometrical defects, particularly in the case of overhang geometry. In such cases, one of the most commonly observed defects is "side loss" (Figure 1). This term was first introduced by Tounsi and Vignat [4] in their experimental study of geometrical defects in the EBM process. The authors reported that the side loss effect cannot be limited by adding classic support structures, unlike warping. Different authors [6, 7] have attributed this defect to inhomogeneous shrinkage between the subsequent layers; they argue that the contraction of the first layers is not inhibited [7], while the contraction of further layers is limited by the previous solidified layers. This leads to a difference in layer length between the first and subsequent layers, and is likely to result macroscopically in the side loss phenomenon.

Another typical defect classically observed in additive manufacturing parts is warping, characterizing the curved shape of the first overhang layers. This defect has been investigated much more in the literature for different additive manufacturing processes [4]–[6], [8]–[10]. The different authors have attributed this defect to the lack of heat dissipation in the powder bed, which is less conductive than the solid material. Thus, during cooling of the upper layers of overhang volume, heat dissipation occurs more quickly on the upper layers than the lower ones, which results in compression of the upper layers [9] and traction of the lower layers. This bending state leads to the typical warping shape of the part. In the powder bed process (laser beam melting and electron beam processes), bending is more noticeable in the lower layers, while the lack of volume in the upper layers is compensated by the powder spread by the rake. Consequently, the bottom of the overhang volume is curved, while the top surface remains horizontal [7], [11] (Figure 1).
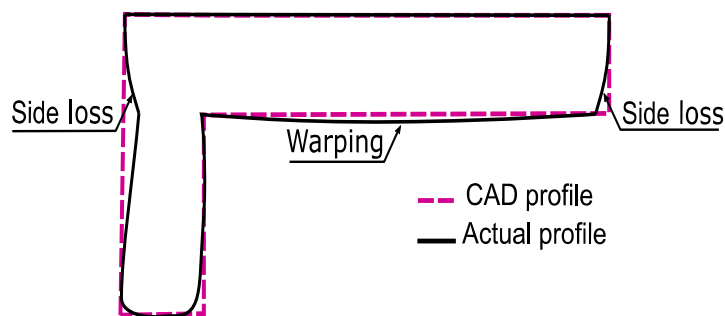
Figure 1: Geometrical defects of overhang part

In the present study, a thermomechanical model is developed in order to simulate side loss defect of overhang parts (schematized in Figure 1). The thermomechanical model represents the actual manufacturing conditions and parameters used to manufacture the parts. The simulated distortions are compared with the distortions of the fabricated parts in order to validate the thermomechanical model. In addition, a batch of overhang parts of different heights is manufactured in order to investigate the effect of overhang height on the side loss amplitude, and thus validate the simulation findings.

2. Analysis of the dominant phenomena and modeling selection

2.1. Description of dominant phenomena

In the EBM process, a typical build starts by creating a vacuum in the building chamber. The electron beam is then used to heat the build plate to 750°C [12]. Powder layers are spread by a rake,

preheated and then melted in particular areas until the complete part is built. The manufacturer ARCAM AB (purchased in 2016 by GE group) proposes various machine models (S12, A1, A2, Q10, etc.), with somewhat different characteristics. In the present study, the samples are made using an ARCAM A1 and EBM control software 3.2. Therefore, the process parameters discussed below are suitable for this machine model.

The electron beam is generated by a tungsten filament [13] and then accelerated using an acceleration voltage of 60kV [14]–[16]. The beam position is controlled using a deflection coil [17], and its size varies as a consequence of the variation of the focus coil field [12]. During the preheat phase, the electron beam heats the powder bed using multiple passes with a high value of current (usually above 30mA [18] [19]) and fast scan rate (about 10^4 mm/s [18], [19]). In the melting phase, the current and the scan rate are reduced respectively to (5mA-20mA) and (100mm/s to 1000mm/s) [19]. The benefits of EBM technology over Laser Beam Melting (LBM), which is the most commonly used metallic powder bed process, include high productivity rate (about 60cm^3/hour [20]), less residual stress and less post-processing. However, EBM remains more complex than laser technology [21], since it requires a vacuum environment and there are more process parameters to optimize [22]. Actually, the EBM process requires three different themes (preheat, support and melting) [11], [23], with each theme defined by several parameters (beam speed, focus offset, line offset, etc.) [11]. The preheat theme is not needed in laser technology, since the SLM powder bed is not preheated before melting, the energy density usually remains constant during the process, resulting in less complexity and fewer parameters to manage.

The process involves several multi-physical interrelated phenomena. These have been classified according to Van Belle [24] into three categories:

- Thermal phenomena: these include melting, solidification and heat dissipation. The heating of the powder bed by the electron beam melts the powder particles [14], [16]. Most of the energy applied by the electron beam is absorbed by the powder material (about 95% [17], [20]). The absorbed energy is then dissipated in the previously deposited dense material mainly by conduction [25] or radiation. The thermal energy in the EBM process results in high temperature gradients and a high cooling rate of approximately 10^3-10^5K/s [25] (obtained for TA6V in EBM) and is the primary source of the mechanical and metallurgical mechanisms discussed later.
- Mechanical phenomena: these include the material constitutive law, stress and strain generated during the process. Generally, in additive manufacturing processes, residual stresses are mainly due to the non-uniform way that the thermal energy is applied to the powder bed [26] and hence the non-uniform expansion and contraction of the material [27]. One of the main advantages of EBM is the ability to produce parts with negligible residual stress, as argued by different authors. Edwards et al. [15] reported the residual stress measured in several EBM samples: the results showed near-zero residual stress in the part. These negligible values can be attributed to the high temperature in the build tank, which continuously relaxes the residual stress in the parts.
- Metallurgical phenomena: these include material composition and crystallographic structure, which depend on the beam intensity [28], scan strategy [27] and build temperature [25] (the surrounding temperature in the build tank).

2.2. Selection of modeling approach

Depending on the modeling scale, material addition in additive manufacturing processes can be modeled using several techniques. Figure 2 sums up the main available techniques proposed in the literature. The selection of one or another technique mainly depends on the scale of the study, the physical phenomena to be modeled, the expected accuracy and the available computing resources. In our case, we use thermo-elastoplastic analysis to simulate the geometrical defects coupled to the "element birth technique" [21], [24], [29]–[31] for the addition of new layers in both thermal and mechanical models. In this technique, the mesh of the complete geometry is created and all elements are initially deactivated. They are then activated gradually during the simulation to represent the addition of the new material. Despite the high computational costs associated with this technique, it remains the most efficient for representing the addition of new layers correctly [24]. To model the phenomena at the melting pool scale, alternative methods use adaptive moving mesh (ALE) [32]–[34], volume of fluid or level set method. At the part scale, commonly used approaches include inherent strain method [35]–[38] and inherent shrinkage technique [39]. These techniques are not detailed here because they are considered beyond the scope of this work.

Side loss defect is mainly due to thermomechanical phenomena during the process; its magnitude varies significantly with the geometry and orientation of the produced parts. To point out and identify the main reasons for the appearance of this defect, in the present work we propose to study a cantilever geometry produced horizontally (as shown in Figure 1). With this particular geometry, side loss can be observed in different zones. First, we study the manufacturing defects experimentally through a batch of parts produced with the same configuration. Next, we set up numerical simulations in order to understand the physical phenomena occurring during the manufacturing process. Currently, the use of numerical models remains limited, mainly due to the computing time required; thus, there are very few thermomechanical simulations in the literature that model the actual size of EBM parts, and even fewer thermomechanical simulations compared to macroscopic geometrical defects. The numerical simulation developed here is based on the Abaqus commercial software through two simulation steps. First, a thermal model is developed in order to evaluate the temperature field during production. In this model, the estimated electron beam energy is gradually applied to the powder layers; the transient temperature is then calculated according to the passage of the electron beam across different layer elements. Temperature field is then used as an input for the mechanical model. The resulting geometrical distortion is then compared to parts produced with the same conditions. From this comparison, we propose to analyze and understand how these defects occur during the deposition of multiple layers.

The main motivation here is to understand the thermo-mechanical phenomena leading to macroscopic distortions of overhang structures, and then to understand the reasons for the appearance and the causes of the geometrical defects observed experimentally on overhang EBM geometries. To do this, it was decided not to model metallurgical transformations at the microscopic scale. The thermal model setup includes the variation of thermal properties caused by state modifications (from powder, to liquid and solid states). The thermal effect of the state modification is modeled by a latent specific heat between solidus and liquidus. The electron heat input is deduced from current intensity, acceleration voltage, powder absorption coefficient and scan rate. Two heat loss sources are considered: i. conduction in the surrounding material, estimated by thermal resistance; ii. radiation using the emissivity of the material. In the mechanical model, it is assumed

that the powder has a marginal effect on geometrical distortion due to the relatively low mechanical property (compared to the dense material). Mechanisms occurring on a smaller scale (capillary forces, Marangoni convection, chemical reactions, etc.) are not addressed in this study.
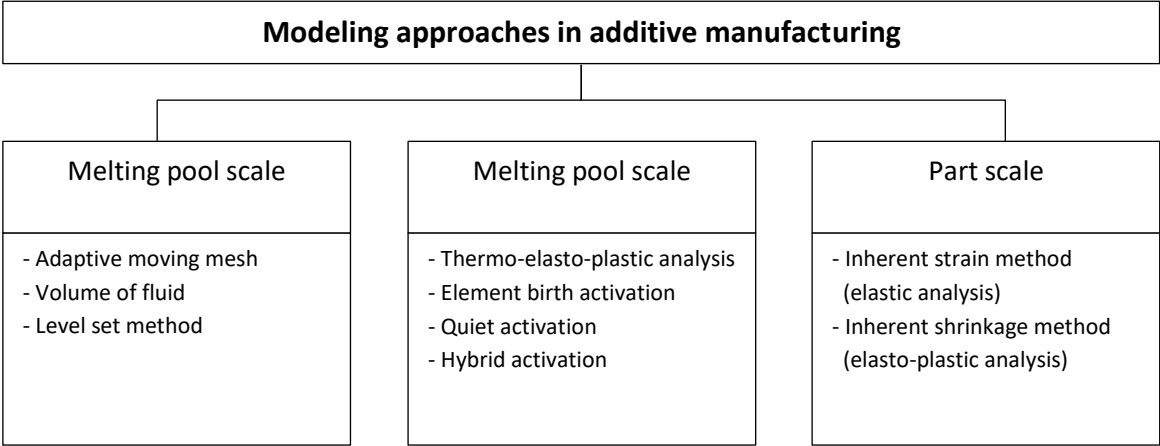
Modeling approaches in additive manufacturing		
Melting pool scale	**Melting pool scale**	**Part scale**

- Adaptive moving mesh
- Volume of fluid
- Level set method
	- Thermo-elasto-plastic analysis
	- Element birth activation
	- Quiet activation
	- Hybrid activation
		- Inherent strain method
		  (elastic analysis)
		- Inherent shrinkage method
		  (elasto-plastic analysis)

Figure 2: Modeling approaches in additive manufacturing processes at different scales

2.3. Geometrical observations on the produced parts

The Titanium based alloy TA6V was used to produce several batches of overhang parts by EBM. All the produced parts present the side loss defect at the free end of the overhang volume. An example of a produced batch is shown in Figure 3 and is composed of 16 parts. Contour support is used to better sustain the overhang portion and avoid warpage. The offset between the parts and the build plate is 3mm and the scanning strategy used during production is shown in Figure 3. In this case, the 16 parts are considered as individual parts. Thus, the electron beam scans along the length of each part (called scan vector) in the considered scan direction, before moving to the next scan vector.
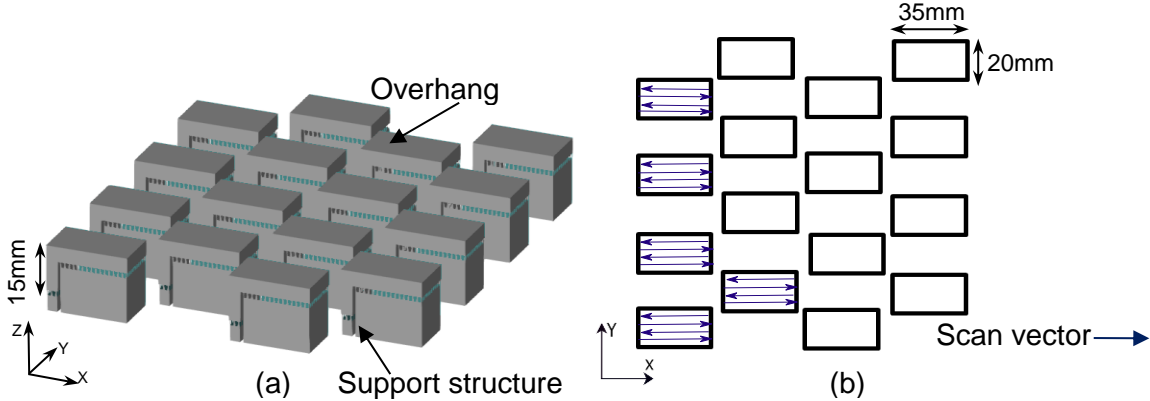
**Figure 3: Batch of overhang parts (a) CAD file (b) Scanning strategy**

Several batches were manufactured under the same conditions. Contour supports were removed from the as-fabricated parts (Figure 4-b). All produced parts have the same shape and present the same geometrical defects. A representative sample is shown in Figure 4. Side loss can be observed on the left horizontal side of the part. At the bottom of the horizontal shape, there is a relatively small amplitude of warping. In addition, the side loss has a regular shape along the Y-axis of Figure 5. To define the amplitude of geometrical defects, measurements were performed by a 3D optical scanner (GOM Atos Core) and the measured geometry corresponds to a structured mesh of cloud of points.

The measured mesh is aligned with the CAD model through a least square association (based on reference planes of the geometry), then the geometrical distance between the measured mesh and the CAD model is calculated in order to quantify the deviations of the measured data. These geometrical deviations are shown in Figure 5 for a representative specimen of the produced batch. As can be seen in this figure, the green zones represent a good agreement between the CAD and the measured geometry. However, the negative deviations (blue zones) along the edges of the overhang volume represent the amplitude of side loss.
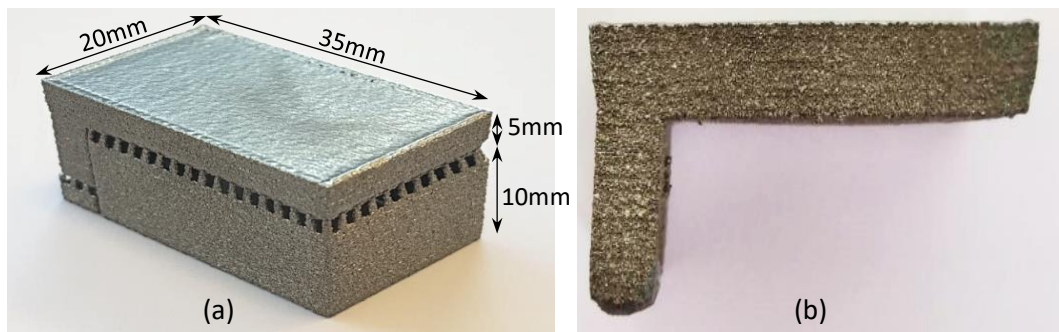
Figure 4: (a) As-fabricated part (with support) (b) Overhang part without support

The measurements confirm the previous global analysis concerning side loss and its regular shape all the way along the edges of the overhang volume ranging from -0.6mm to -0.8mm. Moreover, the same amplitude is observed on the left side of the part. This leads to the conclusion that the side loss is symmetrical and the massive vertical zone of the part (Figure 6-a) has a relatively small influence on the studied defect.
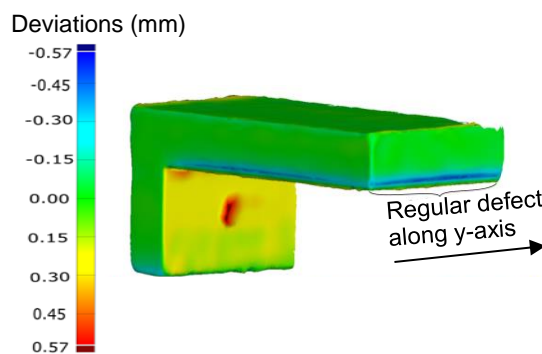
Figure 5: Cartography of geometrical deviations of part No. 2

From the previous geometrical analysis and the shape of the defects, it is considered that the problem is symmetrical and it is therefore sufficient to study half of the part. In fact, the vertical zone of the part seems to have no influence on the amplitude of this defect. The other simplification comes from the process sequence of the electron beam coupled to the part orientation, as shown in Figure 3. Since the electron beam follows the same route to weld the different layers of the part, it is proposed that only a vertical wall on the right half portion of the overhang volume is simulated. In Figure 6, the global geometry of the simulated wall is drawn. The dimensions are 17.5mm x 5mm x 400 µm. The thickness of the wall corresponds to the electron beam diameter.
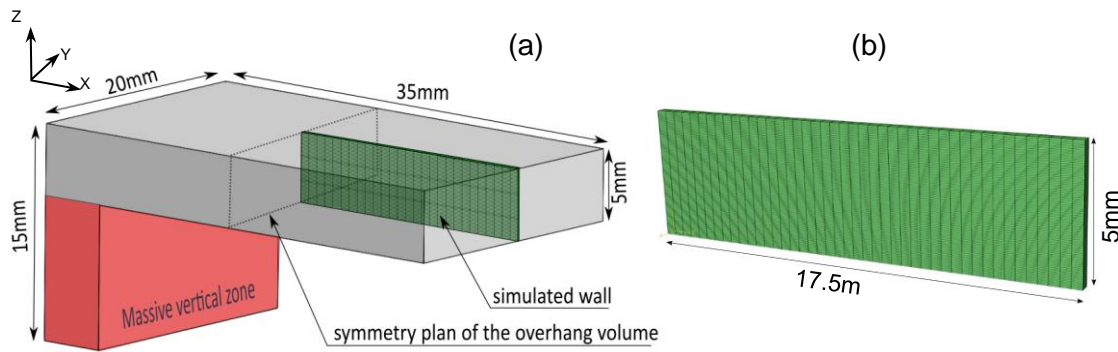
Figure 6: (a) Geometrical model; (b) simulated wall

3. Modeling setup

3.1. Thermal modeling setup

The evolution of the transient temperature field is computed using Abaqus software. As argued in Section 2, the three thermal phenomena to be modeled are the melting of powder material, solidification and heat losses. To do this, the thermal simulation takes into account the following steps:

- Preheating the build plate: the process starts by preheating the build plate, the evolution of the plate temperature during the process is given by the thermocouple located at the bottom of the build plate (Figure 7). The plate is preheated to a temperature of 750°C. This phase is not simulated in the present work and it is assumed that the temperature is 750°C at the beginning of the build.
- Spreading the powder material between the build plate and the overhang volume: the model starts by gradually activating 20 layers of 50µm (thickness of a single layer) to represent the powder material separating the overhang volume from the build plate. Powder layers are activated with a temperature of 750°C respecting raking time (10s) and consolidation time (9s). In all the steps of the simulation, the powder material is considered as continuous media with homogeneous properties.
- Gradual melting of the powder elements: once the powder layers separating the build plate from the overhang part are activated, additional powder layers are gradually activated at preheating temperature. For these new activated layers, the electron beam energy is gradually applied to layer elements. The properties of elements change from powder to solid state according to the position of the electron beam (as shown in Figure 8). In the numerical simulation the activation procedure respects the actual parameters used by the ARCAM build theme, as depicted below.
- Final cooling of the part: after the deposition of all layers, the elements are gradually cooled to room temperature (20°C).

According to these main phases of the build process, it is proposed to simulate production at the end of the preheating phase and after the first consolidated powder deposition. It is then assumed that the first consolidated layers have no effect on the final geometrical defects (due to the low mechanical strength of the material). To introduce the effect of the temperature drop during production, the data recorded by the thermocouple sensor located at the bottom of the build plate (shown in Figure 7) are used directly as a boundary condition. This boundary temperature (referred

as build plate temperature in Figure 8) is updated during the activation of each new layer in order to represent correctly the change of build plate temperature during the fabrication.
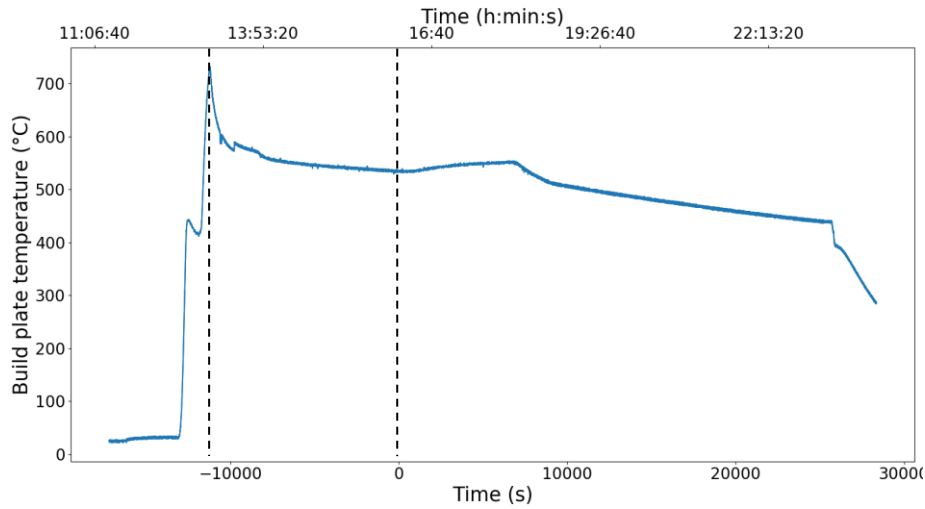

Figure 7: Build plate temperature during the build (experimental data from the manufactured batch).
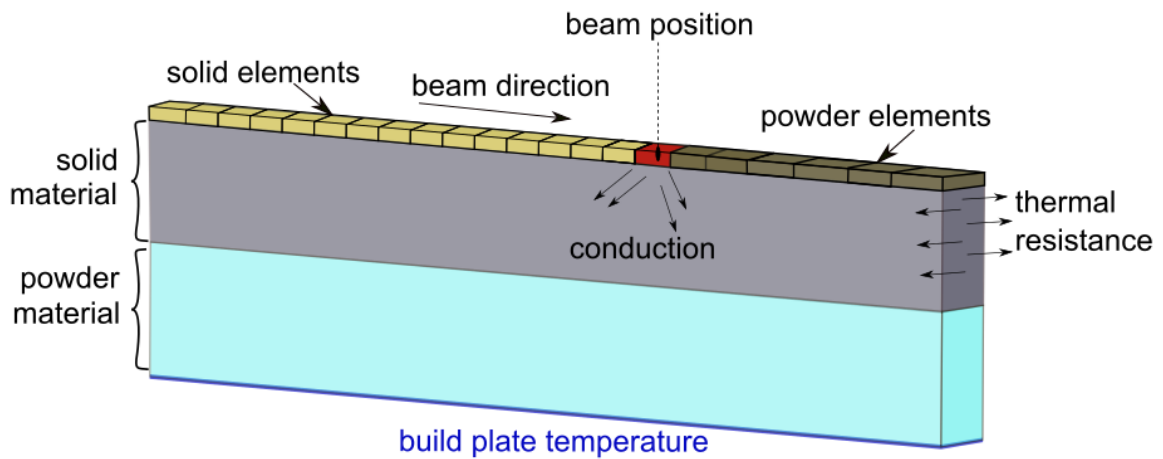

**Figure 8: Schematic representation of thermal model**

The transient temperature is calculated according to the heat transfer equation (Eq 1) which takes into consideration temperature and state-dependent material properties:

$$\rho(T, \alpha) \, C_P \, (T, \alpha) \frac{\partial T}{\partial t} - div \, (k \, (T, \alpha) \, grad \, T) - Q = 0 \qquad \text{Eq 1}$$

Where ρ is the material density, C_P is the specific heat capacity and k thermal conductivity.

Eq 1 shows the dependence of these thermal properties on temperature T and state variable α (α=0 for powder state, and α=1 for dense state). During activation of the entire powder layer, temperature T is equal to 750°C, corresponding to the preheating phase, while the state variable α is equal to 0 to represent the powder state. During scanning, when the temperature of a scanned element exceeds the melting point, the new value of α is set to 1, corresponding to the transition from powder to dense liquid state. During cooling, the temperature drops below the melting point. The thermal characteristics are then set as in solid state. The thermal properties ρ, C_P, k used in the numerical simulation are functions of the actual temperature, as shown in Figure 9. Thus, thermal

properties such as density, conductivity, specific heat capacity and emissivity are plotted for solid, liquid and powder states for temperatures ranging from ambient to melting point of TA6V (1665°C [41], [42]).
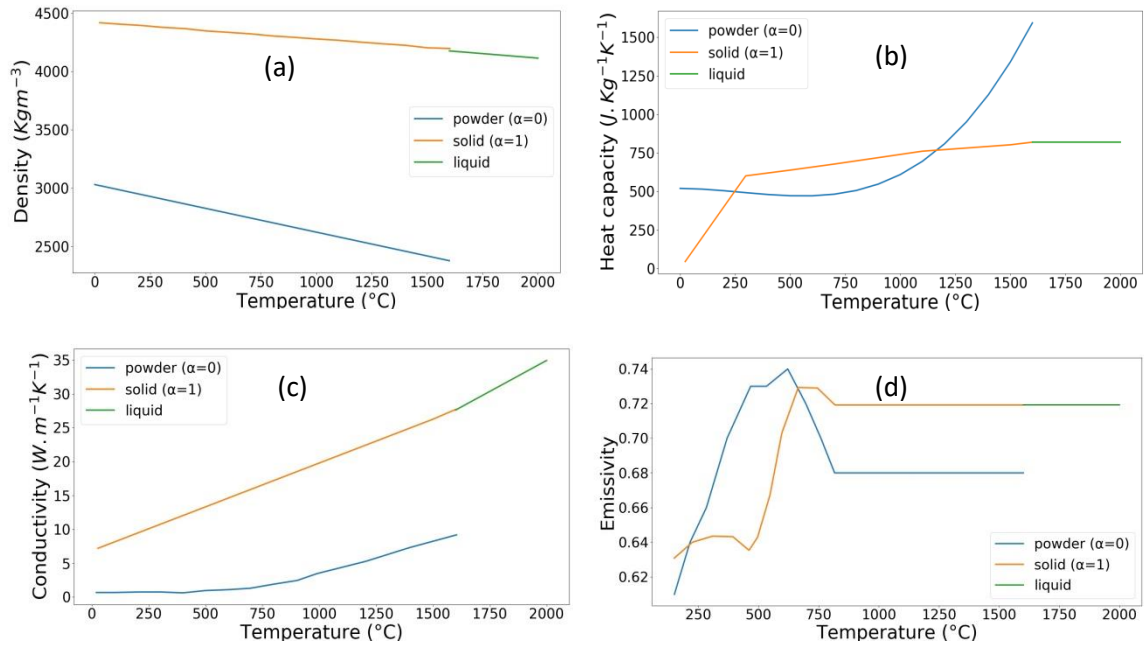
Figure 9: Temperature-dependent thermal properties of TA6V (a) Density [12], [41]; (b) Heat capacity [41]; (c) Conductivity [21]; (d) Emissivity [40]

According to [43–47], the electron beam energy density, Q in Eq 1, is estimated as follows:

$$Q(J/m^3) = \frac{\eta \, U \, I(l)}{\Phi \, p \, V(l, Z)} \qquad \text{Eq 2}$$

Where η = 70% is the efficiency coefficient representing the amount of energy absorbed by powder elements, U=60kV [1, 3, 16] is the accelerating voltage of the electron beam, Φ=400µm [14], [26] is the beam spot diameter, p=100µm is the penetration depth of the electron beam into the layers, l is the scan length and Z the height of the overhang layer. I(l) and V(l,Z) represent respectively the current and the scan speed of the electron beam. These two parameters are continuously changing in the EBM process, they can be determined using ARCAM functions: current compensation, speed function and thickness function. The beam current I depends on the scan length l, and is estimated using the current compensation function. The scan speed V depends on the scan length l and the height of overhang layer Z, and is estimated using speed function and thickness function. Details about the current compensation, speed function and thickness function can be found in [47].

For production, the manufacturing parameters are stored in a typical log file. Based on the ARCAM functions [47] and the log file data, it is possible to determine the volumetric energy to apply to every element according to the number of layers. Figure 10 shows the evolution of the energy level as a function of the layer number. It can be observed that the energy levels change during the first layers, due to the particular strategy of ARCAM to adjust the energy according to the thickness of the part and in this way limit any over-heating phenomena. After the application of the beam energy for a given layer, there is a pause of 50 seconds before the activation of the next layer in

order to represent the required time to melt the other parts. The accumulated heat is then dissipated by conduction and radiation. The bottom nodes of consolidated powder are maintained at the build plate temperature following the curve seen in Figure 7. Thus, by conduction, the new elements exchange heat through previous solid layers and then through consolidated powder layers. The conduction through the surrounding dense material is modeled by a convective coefficient h, assuming equivalence between the conductive and convective thermal resistance (Eq 3).

$$R_{th}^{cond} = \frac{e}{\lambda} = R_{th}^{conv} = \frac{1}{h} \qquad \text{Eq 3}$$

Where e is equal to 10mm (width of half of the part (Figure 6-a)) and λ thermal conductivity of dense material at 550°C.

The energy radiation Q_{rad} is calculated by Eq 4. This heat quantity is temperature-dependent and becomes more significant with high temperature values.

$$Q_{rad} = \varepsilon(T)\sigma \ (T^4 - T_{bc}^4) \qquad \text{Eq 4}$$

Where $\varepsilon(T)$ represents the emissivity of dense material, σ the Stephan-Boltzmann constant and T_{bc} the build tank temperature.
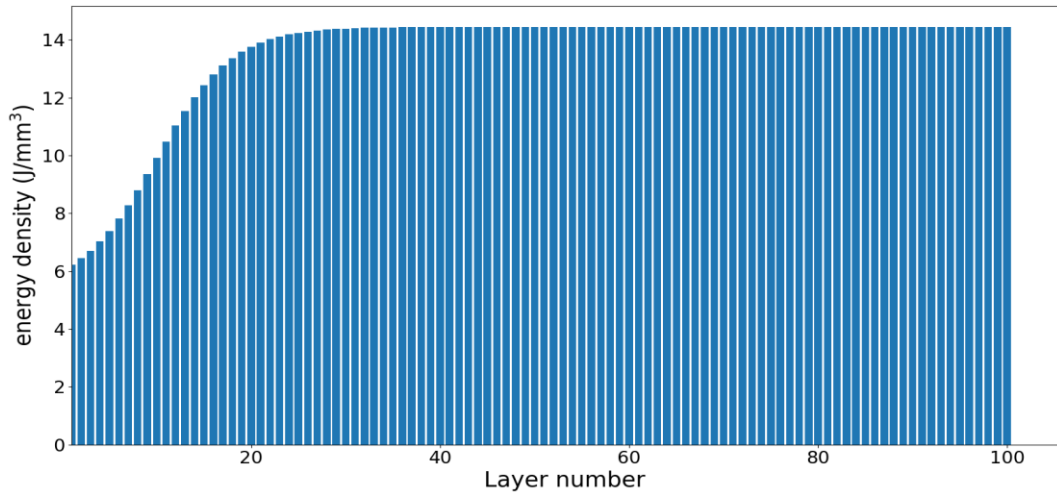

Figure 10: Schematic representation of energy density as a function of layer number

3.2. Mechanical modeling setup

After calculation of thermal history in the thermal model, temperature field is applied successively as an input in the mechanical model following the same activation technique. The activated elements appear in the same order and at the same scan speed as in the thermal model. The powder state is not modeled because of its low mechanical properties compared to solid material. Thus, for each new layer, the elements are successively activated at the temperature imported from the thermal results (usually higher than the melting point). When the temperature drops below the melting point, the elements take on solid material properties and interact mechanically with other elements. Each element is activated without initial displacement, strain or stress. During the activation, the free nodes of elements appear at their initial position (defined by the initial mesh) since the effective position of the solid part is governed by the actual position of the electron beam and not by the deformation of the previous cooling element of the layer. Consequently, the real length of the activated element is different from the initial length of mesh (cumulating the decrease in length of the previously deposited cooling element of the layer).

The mechanical properties used in the model are thermally dependent (i.e. Young modulus and thermal expansion coefficient). According to Shwarnakar et al. [48], a linear dependency can be observed between the Young modulus and the temperature ranging from 20°C to 1000°C. For temperatures over 1000°C, an extrapolation of the previous data is assumed (mainly motivated by the lack of data). The corresponding curve is shown in Figure 11. The thermal expansion coefficient data is considered from ambient to melting temperature based on the previous works of [Vastola et al., 2016] [49].
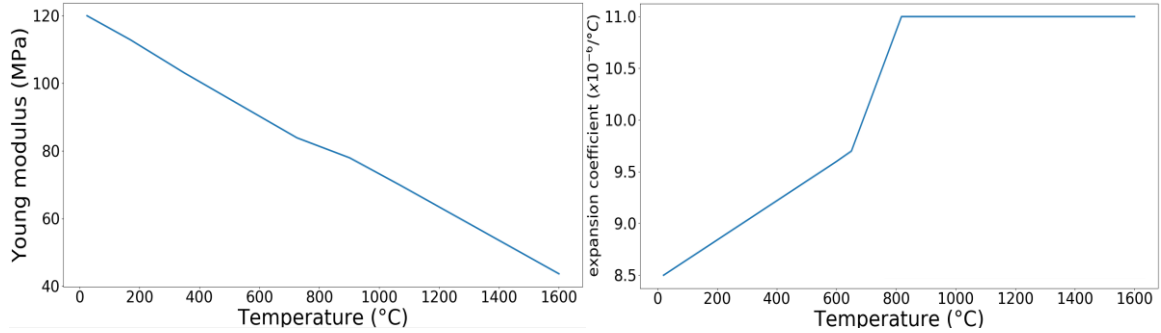
Figure 11: Temperature-dependent mechanical properties of TA6V

It is assumed that the plasticity of the material is governed by a classical Johnson-Cook constitutive law (Eq 5) entirely suitable to represent the thermo-plastic behavior of TA6V alloy [50].

$$\sigma = (A + B\,\varepsilon^n)(1 + C \ln \dot{\varepsilon}^n)\,(1 - T^{*m}) \qquad\qquad \text{Eq 5}$$

The set of parameters used in the model are: A=724.7MPa, B=683.1MPa, C=0.035, m=1, n=0.47. These phenomenological parameters are taken from the work of Lee and Lin [50] for temperatures ranging from 25°C to 1100°C with fixed strain rate of 2×10^3 s^{-1}. It has been shown that there is good agreement between measured and calculated strain-stress values for working temperatures up to 1100°C.

The mesh used for the mechanical model is the same as that used for the thermal study in order to avoid compatibility problems when thermal fields are imported. Thus, the 8-node continuum elements type C3D8 are used. The mechanical boundary conditions in the model are as shown in Figure 12:

- The bottom of the simulated wall is constrained along the Z direction to model the presence of the support structure under the overhang portion of the part.
- The back side is constrained along the Y direction to represent the solid portion of the part already built.
- The left side is blocked along the X direction considering the symmetry of the overhang portion of the part.
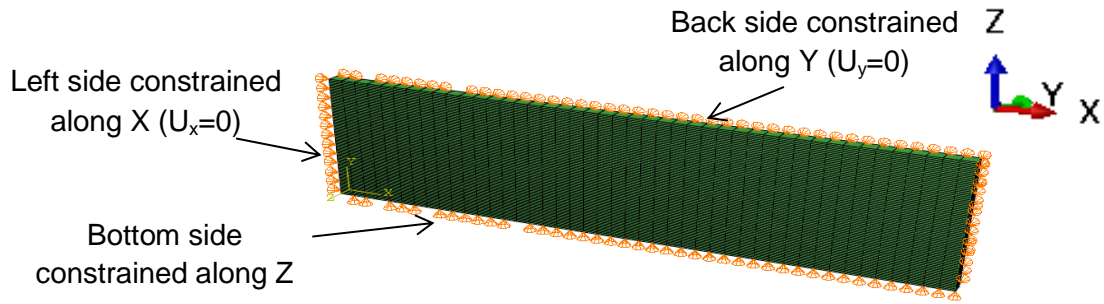
Figure 12: Mechanical boundary conditions

4. Results and discussion

4.1. Thermal results

Figure 13 results from a numerical simulation of temperature history of a particular element in the 30th deposited layer. After activation of the element at 750°C, a rapid rise in temperature can be observed when the beam energy is applied (close to 1750°C). Next, the electron beam moves to neighboring elements (of the same layer), the element temperature decreases gradually until reaching an equilibrium temperature around the build plate temperature.

When beam energy is applied to the element of the next layers (located on the apex of the first studied element), the temperature peak is less than the initial one (close to the fusion temperature). During the next layer depositions, the temperature gradually decreases towards an asymptotic value close to the bottom plate temperature (550°C).
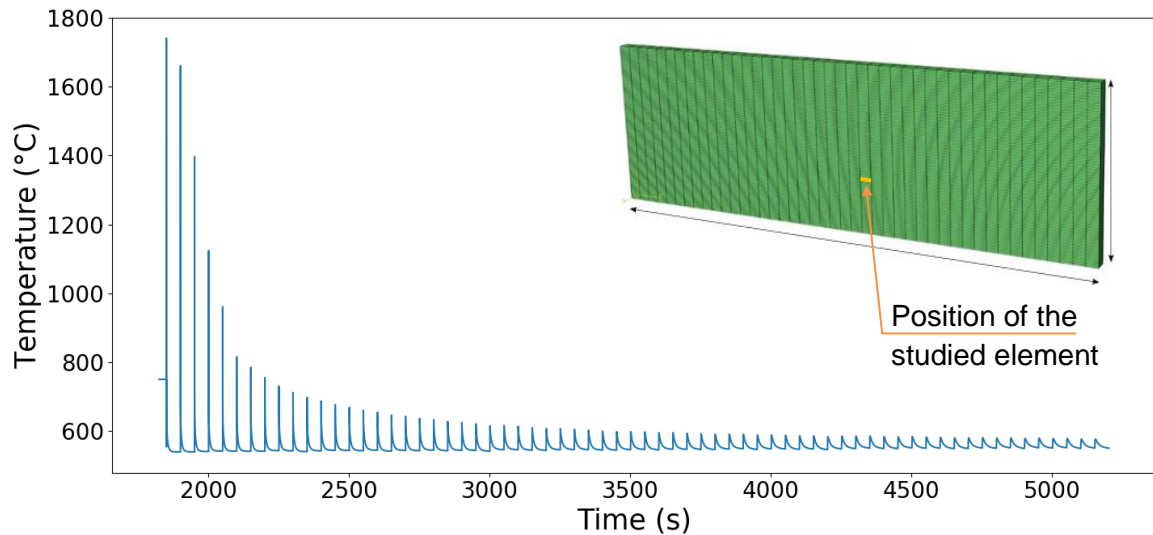

Figure 13: Example of temperature history

According to the numerical simulation, the melting pool dimensions vary depending on the height of the deposited layer. They are very localized between the 1st layer (0.05mm of overhang height) and the 20th layer (1mm of overhang height). For example, after deposition of 10 layers the length and width of the melting pool are about 1.2mm and 50µm respectively (Figure 14), increasing to 3.6mm and 70µm after the 50th layer (about 2.5mm of overhang). This phenomenon could be explained by the energy adjustment for the first deposited layer and when the number of layers is large enough; since the energy range remains at the same level and exchange conditions are similar, the melting process has a similar influence on the heat-affected area. In the present work, the

thermal results are used as an input for mechanical simulation and are not the main concern of this study. For this reason, the analysis of the effect of ARCAM functions on thermal analysis is not detailed. Moreover, the experimental validation of thermal results is not addressed here, and will be the subject of further studies.
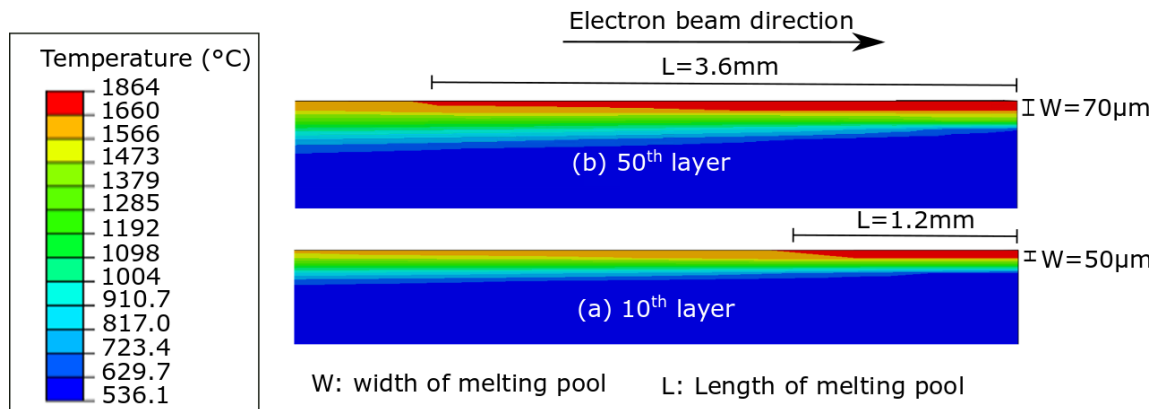

Figure 14: Magnification of heat affected area after deposition of 10 layers (a) and 50 layers (b)

4.2. Mechanical results

The fast thermal cycles in the part result in non-negligible geometric distortions. These distortions take place gradually during the successive energy depositions and cooling of elements for the successive layers (corresponding to steps in the numerical simulation). Figure 15 shows the displacement history of the last activated element of the 1st, 20th, 40th, 60th, and 80th layers. The initial position of the mesh is taken as a reference to calculate element displacement (Figure 15 (a)). Since the elements are activated at their maximum temperature, and without any strain or stress, the initial value of displacement is zero at activation (Figure 15 (b)). All the curves decrease as a function of time (i.e. negative values of displacements) and periodic peaks could be observed (every 50s) corresponding to the energy deposition and cooling phase on the particular element (Figure 15 (b)).

For the first element of the first layer, the initial position is 0mm, meaning that, at the activation time, the temperature is higher than the melting point. Then, during the 50s after this activation time, the position of this element decreases until it reaches -0.1mm due to shrinkage. With the next energy deposition, the position increases to -0.08mm (assuming a drop in temperature close to the melting point and expansion phenomena). The next cooling phase moves the position of the element close to -0.16mm. The same process and phase is achieved for all cycles of production (melting material and cooling phase). Finally, the displacement range of this first element starts from 0mm and reaches -0.77mm at the end of the simulation.

We draw the displacements as the function of the simulation time of the last elements of the 1st, 20th, 40th, 60th and 80th layers, respectively designated by U_1^{max}, U_{20}^{max}, U_{40}^{max}, U_{60}^{max} and U_{80}^{max} (Figure 15 (b)). From these displacement curves, the final displacement of the part is due to the local shrinkage of every layer amplified by the shrinkage of the layers above. This phenomenon is explained by the two main stages repeated every 50s: activation at a temperature higher than the melting point and the cooling stage. During activation of the elements, the local temperature rise leads to thermal expansion of the zone and to a tensile stress state in the previous solid layers. During the cooling stage, the shrinkage of the last layer leads to a compressive stress state in the previous solid layers and in turn, to a decrease in position.

The displacement curves in Figure 15 (b) show a difference in displacement histories for the different layers. This difference illustrates the influence of the overhang height (or number of layers) on the final distortion of the part. For example, the displacement at the end of the first layer U_1^{max} shows a more significant decrease during activation of the first 60 layers (during the first 3000s of the build), this can be explained by the large number of solidified layers (after the 60th layer) which are harder to compress during the shrinkage of the last layers. Accordingly, after 60 layers, displacement at the end of the first layer U_1^{max} decreases slightly and stabilizes around -0.7mm.

After deposition of the next layers, the displacement histories U_{20}^{max}, U_{40}^{max}, U_{60}^{max} and U_{80}^{max} have the same trend as U_1^{max}. In Figure 15 (a), it can be observed that the displacement of the right side of the part has an asymptotic behavior since the number of solidified layers (hence, their rigidity) limits the displacement and results in less deformation along the layers.

(a)

(b)
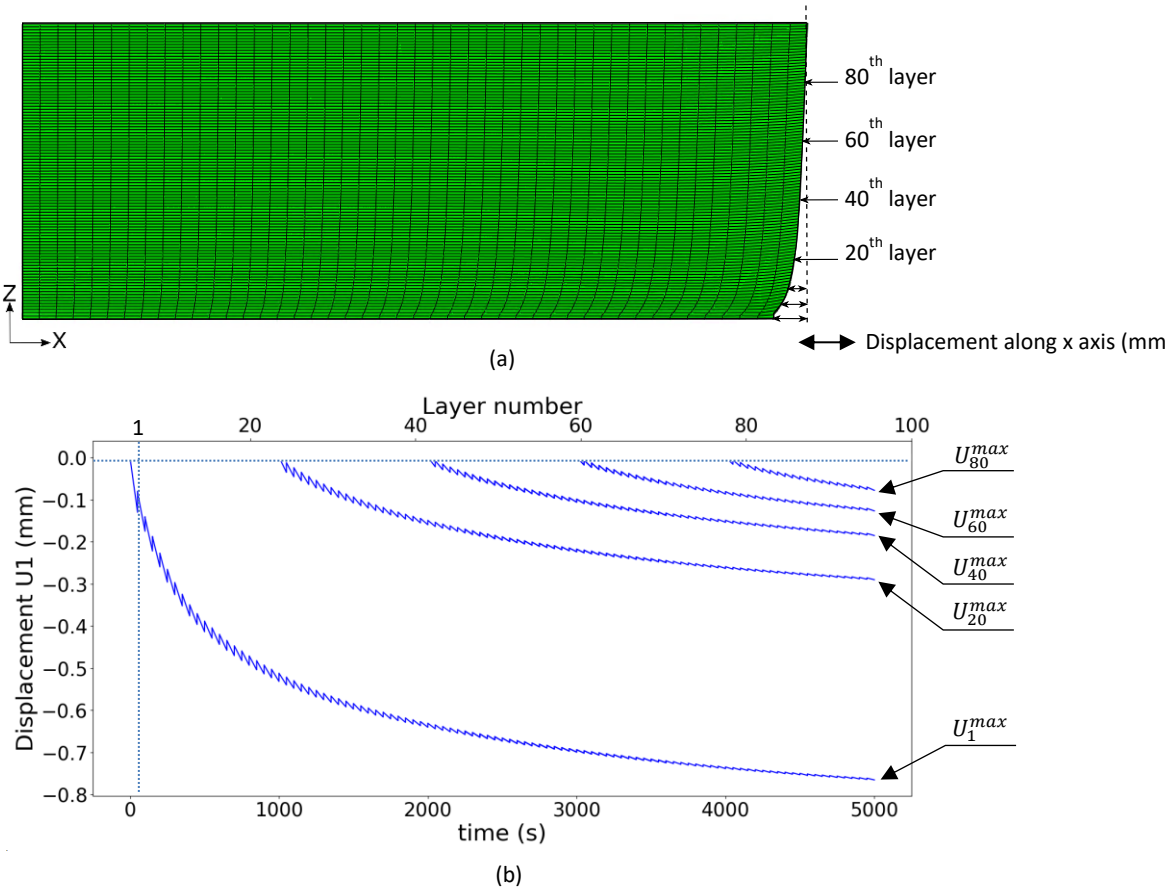
Figure 15: Displacement history at the end of the deposition of different layers

Consequently, the side loss defect results from the successive shrinkage of elements and the accumulated residual stress state of the different layers. Mechanical results show a gradual evolution of side loss from the first layer to the last; the amplitude of the side loss is characterized by the displacement at the end of the deposition of the first layer, referred to as U_1^{max} in Figure 16. For example, the side loss amplitude after the deposition of the first layer is U_1^{max}=-0.13mm, this value continues to increase after the deposition of the next layers, reaching -0.57m after the 20th layer, -0.68mm after the 40th layer, and stabilizing around -0.7mm after the deposition of the 60th layer.

After the deposition of the first layer, the shrinkage of elements results in a small displacement value (U_1^{max}=-0.16mm). As the next layers cool, they apply a compressive stress on the first layer, which leads to a gradual increase in the defect amplitude as the number of layers increases. Also, the tensile stress applied by the first layers on the later ones inhibits shrinkage in the last millimeters and causes a stabilization of the defect after 3mm of height (60th layer). This stabilization can be seen in the simulation results from the vertical shape of the part after 3mm of height, as well as the stabilization of the amplitude at around -0.7mm after this height.
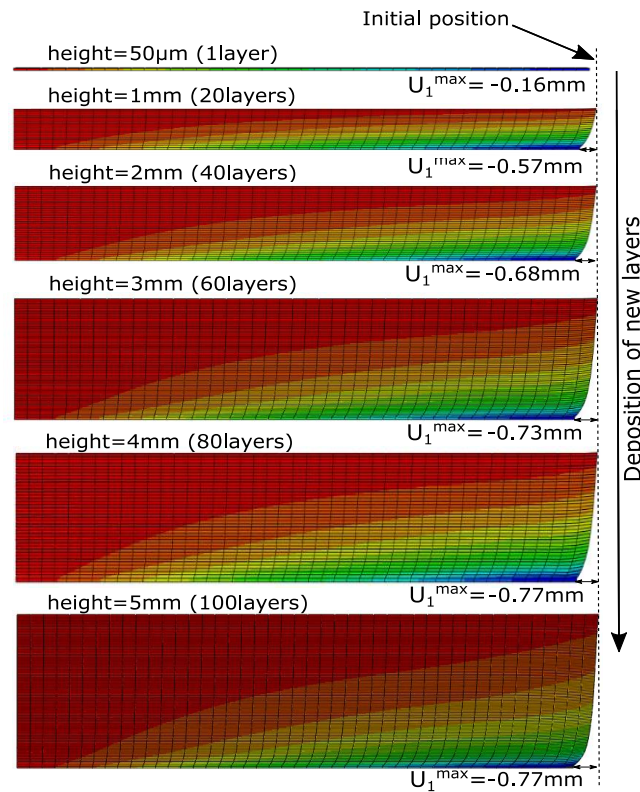
Figure 16: Evolution of cumulated displacement

According to the previous results, the following two findings must be pointed out:

(a) The defect amplitude increases significantly in the first millimeters, and stabilizes after approximately 3mm of height.

(b) The amplitude of side loss depends on the thickness of the overhang volume. Thus, the thicker the overhang volume, the higher the amplitude of the defect.

4.3. Experimental validation

a. Comparison with measured defects

In order to validate the results presented previously, the 16 parts presented in Section 3 were measured using an optical scanner (GOM ATOS Core) and then compared to the numerical results. The 16 produced parts show geometrical defects of similar shape. Side loss varies from –0.6mm to -0.8mm for all 16 parts, against a simulated value of -0.77mm. Generally, the difference in side loss amplitude in EBM processes can be related to the position of the parts in the build plate, as shown in the work of Ghaoui et al. [51] for a similar part geometry. The parts at the border of the build plate

present defects with higher amplitudes than the parts located in the middle of the build plate. This is probably due to the modification of the thermal conditions according to the part position. These phenomena are not considered in the present numerical modeling.

Figure 17 shows a comparison between a measured profile and the shape obtained by the numerical simulation. The superposition of the two profiles shows good agreement between the actual and simulated side loss defects. The global shape of the defect is captured. It should be noted that in the simulation, the bottom of the negative surface is constrained along the Z-axis in order to reduce model complexity. This hypothesis avoids the round shape (called thickness variation) of the profile. It can be seen that in both the simulated and experimental profiles the upper side of the part remains in the horizontal position (for Z=0) with no warping.
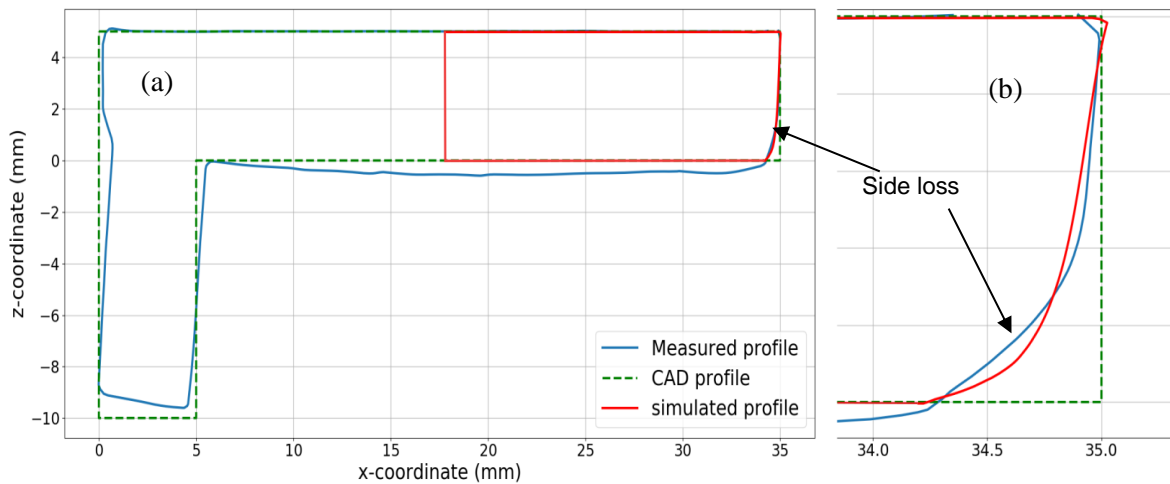
Figure 17: Comparison with experimental data (a) Complete 2D profile (b) Magnification of side loss

b. Influence of part thickness

To experimentally investigate the influence of part height on the side loss phenomenon, 8 parts of different heights were produced using the same process parameters as for the previous 16 parts (EBM parameters). The purpose of carrying out this experiment is to verify the dependency of side loss amplitude as a function of part height (the asymptotic behavior of this defect) and thus test the accuracy of the global numerical simulation in terms of defect predictions since for the first layers, the temperature and the manufacturing process change drastically. Figure 18 shows the produced parts with the same dimensions as the previous produced parts (length and width) and different heights of overhang volume (0.5mm, 1mm, 1.5mm, 2mm, 2.5mm, 3mm, 4mm and 5mm). TA6V alloy is used for the parts with the same scanning strategy and support structure as described in Section 2. The distance between the parts is 3mm and the distance from the build plate is 3mm.

The 8 parts are measured with the 3D optical scanner and are aligned with their respective CAD models, for a better comparison between the measured profiles. Figure 19 shows the different profiles. By comparing side loss in the 8 profiles, it can be seen that thicker parts present defects with higher amplitudes compared to thin parts. The parts with heights less than 3mm have side loss with an inclined shape. Thus, the asymptotic behavior of the side loss is not easy to observe. For other parts (thicknesses of 4mm and 5mm), the defect seems to stabilize in the last layers. Regarding the different heights of the parts, the power of the electron beam is adjusted automatically by the

machine to compensate for the difference in scan lengths. Consequently, a refinement of simulation parameters is required for a quantitative comparison. On this basis, the actual comparisons remain quantitative to validate the global tendency of the side loss and to have a better understanding of the appearance conditions and its evolution during the process.
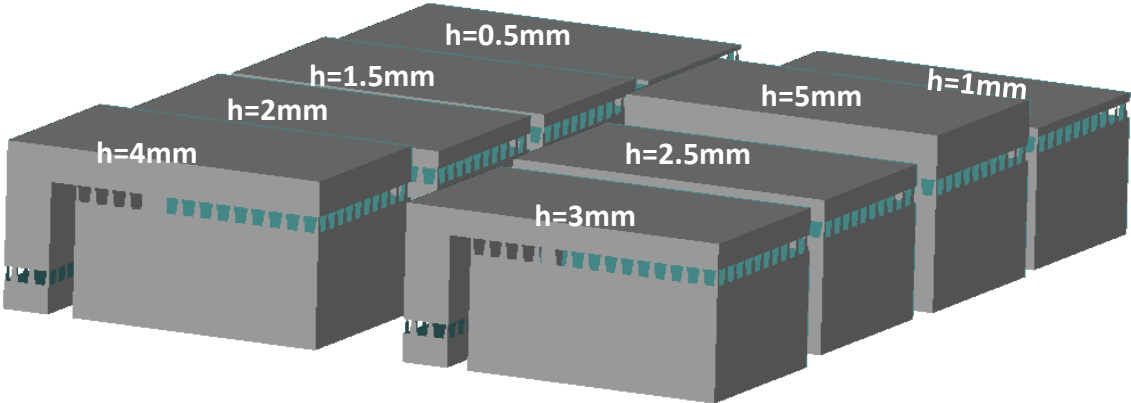

Figure 18: Manufactured parts with different overhang volume heights (h)
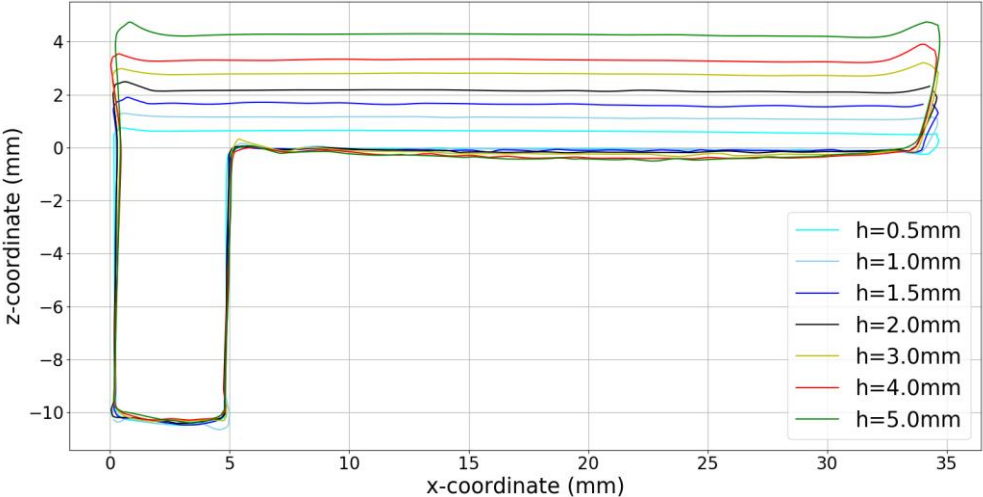

Figure 19: 2D measured profiles of parts with different overhang heights

5. Conclusion

Side loss is a geometrical defect that occurs in overhang structures in additive manufacturing processes. This kind of geometrical defect limits the use of such processes to fabricate large volumes of net-shaped parts with complex geometries without any additional manufacturing finishing operations. In the present paper, we investigate the electron beam melting process with TA6V alloy to understand the mechanisms of the appearance of this defect. Two main approaches are followed based on experimental studies and thermo-mechanical simulations in different manufacturing conditions.

For this purpose, the raking, melting and cooling of powder layers are simulated in a thermal model representing the actual parameters of the process. The temperature evolution is used as input conditions for the mechanical model to simulate the "side loss" defect caused directly by thermo-mechanical phenomena. Optical scanning was used for the experimental measurements of the

produced parts. The profiles of the real and simulated parts are compared directly and the shapes of the overhang geometry are found to be quite similar.

First results of this analysis show that side loss is due to shrinkage of deposited layers and this effect is amplified by intra-layer interactions since the compression of the new layers during cooling increases the defect amplitude; the tensile stress state in the previously deposited layers inhibits the upper shrinkage and results in the stabilization of the defect after a few millimeters of height. The influence of part height is limited, and after 3mm side loss has an asymptotic behavior. To confirm the assumption on the influence of layer shrinkage, parts were built using the same manufacturing conditions, with different overhang heights. The thermomechanical model developed here can be used to predict the side loss defect for other sizes of overhang volume. These results can then be used to pre-compensate the STL-file, in order to avoid defect formation, and therefore produce parts with better geometrical quality. The STL file can be pre-compensated by scaling up the first layers progressively, according to the simulation results.

This original work gives an understanding of the phenomena responsible for side loss, however, there are some limitations. The first concerns the exact identification of the energy deposition. According to the ARCAM manual, functions are used to adjust the energy level according to scan length, part thickness, etc. These complex and usually correlated functions make it more difficult to clearly identify the final temperature of the melting material. For this purpose, an in-depth analysis of the functions used is in progress. Also, we will equip the ARCAM machine with thermocouples to confirm the way the energy is applied throughout the fabrication process.

The second limitation directly concerns the boundary conditions of the simulation. To obtain a good balance between computing time and simulation accuracy, an equivalent value of the resistance interface is introduced. From this assumption, it is only possible to manage a wall of elements representative of the produced part. Even if the assumption on the boundary conditions is used in the traditional way, this is accurate for steady conditions but not for dynamic phenomena. Some additional simulations should be run to identify the influence of this assumption on the final part shape computed by the numerical simulation.

Finally, during the entire production process, the material is maintained at a high temperature (for TA6V, close to 750°C). Under these thermal conditions, the residual stress state, responsible for the geometrical defects, should decrease in a short time and this corresponds to a classical thermal annealing process. According to the literature, for this alloy and these thermal conditions, the annealing process is performed in a few minutes. This could lead to some difference in the final simulated shape of the defects. These next improvements are in progress and will complement these first major results on the global defects produced in manufactured parts.

References

[1] C. Körner, "Additive manufacturing of metallic components by selective electron beam melting — a review," International Materials Reviews, vol. 61, no. 5, pp. 361–377, Jul. 2016, doi: 10.1080/09506608.2016.1176289.

[2] "Arcam EBM A2 User's Manual", 2007.

[3] E. Malekipour and H. El-Mounayri, "Common defects and contributing parameters in powder bed fusion AM process and their classification for online monitoring and control: a review," Int J Adv Manuf Technol, vol. 95, no. 1, pp. 527–550, 2018, doi: 10.1007/s00170-017-1172-6.

[4] R. Tounsi and F. Vignat, "New concept of support structures in Electron Beam Melting manufacturing to reduce geometric defects - Experimental investigation," presented at the 15e Colloque National AIP-Primeca, 2017, pp. 1–6.

[5] C. Schmutzler, A. Zimmermann, and M. F. Zaeh, "Compensating Warpage of 3D Printed Parts Using Free-form Deformation," Procedia CIRP, vol. 41, pp. 1017–1022, 2016, doi: 10.1016/j.procir.2015.12.078.

[6] Christoph Schmutzler, Fabian Bayerlein, Stephan Janson, Christian Seidel, and Michael F. Zaeh, "Pre-compensation of Warpage for Additive Manufacturing," JMEA, vol. 6, no. 8, 2016, doi: 10.17265/2159-5275/2016.08.002.

[7] P. Vora, F. Derguti, K. A. Mumtaz, I. Todd, and N. Hopkinson, "Investigating a Semi-Solid Processing technique using metal powder bed Additive Manufacturing Processes," Proceedings Solid Freeform Fabrication Symposium, 2013.

[8] K. Cooper, P. Steele, B. Cheng, and K. Chou, "Contact-Free Support Structures for Part Overhangs in Powder-Bed Metal Additive Manufacturing," Inventions, vol. 3, no. 1, p. 2, 2018, doi: 10.3390/inventions3010002.

[9] B. Cheng and K. Chou, "Geometric consideration of support structures in part overhang fabrications by electron beam additive manufacturing," Computer-Aided Design, vol. 69, pp. 102–111, 2015, doi: 10.1016/j.cad.2015.06.007.

[10] U. Umer et al., "Modeling the Effect of Different Support Structures in Electron Beam Melting of Titanium Alloy Using Finite Element Models," Metals, vol. 9, no. 7, p. 806, 2019, doi: 10.3390/met9070806.

[11] L. Yang et al., Additive Manufacturing of Metals: The Technology, Materials, Design and Production. Springer International Publishing, 2017.

[12] N. Béraud, "Fabrication assistée par ordinateur pour le procédé EBM", PhD thesis, 2016.

[13] M. Jamshidinia, F. Kong, and R. Kovacevic, "Numerical Modeling of Heat Distribution in the Electron Beam Melting® of Ti-6Al-4V," J. Manuf. Sci. Eng, vol. 135, no. 6, 2013, doi: 10.1115/1.4025746.

[14] M. Galati and L. Iuliano, "A literature review of powder-based electron beam melting focusing on numerical simulations," Additive Manufacturing, vol. 19, pp. 1–20, 2018, doi: 10.1016/j.addma.2017.11.001.

[15] P. Edwards, A. O'Conner, and M. Ramulu, "Electron Beam Additive Manufacturing of Titanium Components: Properties and Performance," Journal of Manufacturing Science and Engineering, vol. 135, no. 6, p. 061016, 2013, doi: 10.1115/1.4025773.

[16] E. ATTAR, "Simulation of Selective Electron Beam Melting Processes", PhD thesis, 2011.

[17] A. Ataee, Y. Li, G. Song, and C. Wen, "Metal scaffolds processed by electron beam melting for biomedical applications," Metallic Foam Bone, pp. 83–110, 2017, doi: 10.1016/B978-0-08-101289-5.00003-2.

[18] L. E. Murr et al., "Metal Fabrication by Additive Manufacturing Using Laser and Electron Beam Melting Technologies," Journal of Materials Science & Technology, vol. 28, no. 1, pp. 1–14, 2012, doi: 10.1016/S1005-0302(12)60016-4.

[19] K. Puebla, L. E. Murr, S. M. Gaytan, E. Martinez, F. Medina, and R. B. Wicker, "Effect of Melt Scan Rate on Microstructure and Macrostructure for Electron Beam Melting of Ti-6Al-4V," Materials Sciences and Applications, vol. 3, no. 5, pp. 720–726, 2012, doi: 10.4236/msa.2012.35038.

[20] J. Hiemenz, "Electron Beam Melting," Advanced Materials & Processes, vol. 165, no. 3, pp. 45–46, 2007.

[21] C. H. Y. Fu and Y. B. Guo, "3-dimensional finite element modeling of selective laser melting Ti-6Al-4V alloy," 2014, pp. 1129–1144.

[22] P. Konda Gokuldoss, S. Kolla, and J. Eckert, "Additive Manufacturing Processes: Selective Laser Melting, Electron Beam Melting and Binder Jetting—Selection Guidelines," Materials (Basel), vol. 10, no. 6, 2017, doi: 10.3390/ma10060672.

[23] V. W. smann, P. Drescher, R. Bader, H. Seitz, H. Hansmann, and N. Laufer, "Comparison of Single Ti6Al4V Struts Made Using Selective Laser Melting and Electron Beam Melting Subject to Part Orientation," Metals, vol. 7, no. 3, p. 91, 2017, doi: 10.3390/met7030091.

[24] L. VAN BELLE, "Analyse, modélisation et simulation de l'apparition de contraintes en fusion laser métallique", PhD thesis, 2013.

[25] S. Liu and Y. C. Shin, "Additive manufacturing of Ti6Al4V alloy: A review," Materials & Design, vol. 164, p. 107552, 2019, doi: 10.1016/j.matdes.2018.107552.

[26] M. F. Zäh and S. Lutzmann, "Modelling and simulation of electron beam melting," Production Engineering, vol. 4, no. 1, pp. 15–23, 2010, doi: 10.1007/s11740-009-0197-6.

[27] L. Parry, I. A. Ashcroft, and R. D. Wildman, "Understanding the effect of laser scan strategy on residual stress in selective laser melting through thermo-mechanical simulation," Additive Manufacturing, vol. 12, pp. 1–15, 2016, doi: 10.1016/j.addma.2016.05.014.

[28] S. Bontha and N. W. Klingbeil, "Thermal Process Maps for Controlling Microstructure in Laser-Based Solid Freeform Fabrication 219," 2003, doi: http://dx.doi.org/10.26153/tsw/5557.

[29] J. Ding et al., "Thermo-mechanical analysis of Wire and Arc Additive Layer Manufacturing process on large multi-layer parts," Computational Materials Science, vol. 50, no. 12, pp. 3315–3322, 2011, doi: 10.1016/j.commatsci.2011.06.023.

[30] I. A. Roberts, C. J. Wang, R. Esterlein, M. Stanford, and D. J. Mynors, "A three-dimensional finite element analysis of the temperature field during laser melting of metal powders in additive layer manufacturing," International Journal of Machine Tools and Manufacture, vol. 49, no. 12, pp. 916–923, 2009, doi: 10.1016/j.ijmachtools.2009.07.004.

[31] A. Ponnambalam, B. Esakki, and C. Udayagiri, "Investigation on multi-layer selective inhibition sintering process using finite element analysis," Materials Today: Proceedings, vol. 4, no. 2, Part A, pp. 2439–2444, 2017, doi: 10.1016/j.matpr.2017.02.095.

[32] J. Song et al., "Numerical and experimental study of laser aided additive manufacturing for melt-pool profile and grain orientation analysis," Materials & Design, vol. 137, pp. 286–297, 2018, doi: 10.1016/j.matdes.2017.10.033.

[33] M. Dal and R. Fabbro, "An overview of the state of art in laser welding simulation," Optics & Laser Technology, vol. 78, pp. 2–14, 2016, doi: 10.1016/j.optlastec.2015.09.015.

[34] M. Medale, C. Touvrey, and R. Fabbro, "An axi-symmetric thermo-hydraulic model to better understand spot laser welding," European Journal of Computational Mechanics, vol. 17, no. 5–7, pp. 795–806, 2008, doi: 10.3166/remn.17.795-806.

[35] Y. Ueda and M. G. Yuan, "Prediction of Residual Stresses in Butt Welded Plates Using Inherent Strains," J. Eng. Mater. Technol., vol. 115, no. 4, p. 417, 1993, doi: 10.1115/1.2904240.

[36] M. Bugatti and Q. Semeraro, "Limitations of the inherent strain method in simulating powder bed fusion processes," Additive Manufacturing, vol. 23, pp. 329–346, Oct. 2018, doi: 10.1016/j.addma.2018.05.041.

[37] X. Liang, Q. Chen, L. Cheng, Q. Yang, and A. To, "A MODIFIED INHERENT STRAIN METHOD FOR FAST PREDICTION OF RESIDUAL DEFORMATION IN ADDITIVE MANUFACTURING OF METAL PARTS," p. 7.

[38] I. Setien, M. Chiumenti, S. van der Veen, M. San Sebastian, F. Garciandía, and A. Echeverría, "Empirical methodology to determine inherent strains in additive manufacturing," Computers & Mathematics with Applications, vol. 78, no. 7, pp. 2282–2295, Oct. 2019, doi: 10.1016/j.camwa.2018.05.015.

[39] A. Mendizabal, J. B. González-Díaz, M. San Sebastián, and A. Echeverría, "Improved Accuracy of the Inherent Shrinkage Method for Fast and More Reliable Welding Distortion Calculations," J. of Materi Eng and Perform, vol. 25, no. 7, pp. 2670–2678, 2016, doi: 10.1007/s11665-016-2116-2.

[40] J. Romano, L. Ladani, and M. Sadowski, "Thermal Modeling of Laser Based Additive Manufacturing Processes within Common Materials," Procedia Manufacturing, vol. 1, pp. 238–250, Jan. 2015, doi: 10.1016/j.promfg.2015.09.012.

[41] A. Neira Arce, "Thermal Modeling and Simulation of Electron Beam Melting for Rapid Prototyping on Ti6Al4V Alloys", PhD thesis, 2012.

[42] H. Choo et al., "Effect of laser power on defect, texture, and microstructure of a laser powder bed fusion processed 316L stainless steel," Materials & Design, vol. 164, p. 107534, 2019, doi: 10.1016/j.matdes.2018.12.006.

[43] J. Ciurana, L. Hernandez, and J. Delgado, "Energy density analysis on single tracks formed by selective laser melting with CoCrMo powder material," 2013.

[44] C. J. Smith et al., "Dimensional accuracy of Electron Beam Melting (EBM) additive manufacture with regard to weight optimized truss structures," Journal of Materials Processing Technology, vol. 229, pp. 128–138, 2016, doi: 10.1016/j.jmatprotec.2015.08.028.

[45] L. Thijs, F. Verhaeghe, T. Craeghs, J. V. Humbeeck, and J.-P. Kruth, "A study of the microstructural evolution during selective laser melting of Ti–6Al–4V," Acta Materialia, vol. 58, no. 9, pp. 3303–3312, 2010, doi: 10.1016/j.actamat.2010.02.004.

[46] H. Attar, M. Calin, L. C. Zhang, S. Scudino, and J. Eckert, "Manufacture by selective laser melting and mechanical behavior of commercially pure titanium," Materials Science and Engineering: A, vol. 593, pp. 170–177, 2014, doi: 10.1016/j.msea.2013.11.038.

[47] WILLIAM JAMES SAMES V, "ADDITIVE MANUFACTURING OF INCONEL 718 USING ELECTRON BEAM MELTING: PROCESSING, POST PROCESSING, & MECHANICAL PROPERTIES", PhD thesis, 2015

[48] A. K. Swarnakar, O. van der Biest, and B. Baufeld, "Young's modulus and damping in dependence on temperature of Ti–6Al–4V components fabricated by shaped metal deposition," J Mater Sci, vol. 46, no. 11, pp. 3802–3811, Jun. 2011, doi: 10.1007/s10853-011-5294-1.

[49] G. Vastola, G. Zhang, Q. X. Pei, and Y.-W. Zhang, "Controlling of residual stress in additive manufacturing of Ti6Al4V by finite element modeling," Additive Manufacturing, vol. 12, pp. 231–239, Oct. 2016, doi: 10.1016/j.addma.2016.05.010.

[50] W.-S. Lee and C.-F. Lin, "Plastic deformation and fracture behaviour of Ti–6Al–4V alloy loaded with high strain rate under various temperatures," Materials Science and Engineering: A, vol. 241, no. 1, pp. 48–59, 1998, doi: 10.1016/S0921-5093(97)00471-1.

[51] S. Ghaoui, Y. Ledoux, and A. Ballu, "Analyse de la variation géométrique des pièces produites en fabrication additive EBM - Cas de pièces avec volume surplombant" in 16e Colloque National S-mart, 2019.